

Passivating pinholes for large-area and high-efficiency silicon solar cells with tunnel oxide passivated contact

Received: 29 November 2024

Accepted: 27 February 2026

Published online: 14 March 2026

Check for updates

Wenqian Zhang^{1,5}, Kangping Zhang^{2,5}, Yuhua Bai^{1,5}, Yuanyuan Zhang^{1,5}, Kuan Yang¹, Bingbing Chen¹, Xueliang Yang¹, Jiadong Li², Yanan Sun², Yan Wu², lingzhi Li², Xuning Zhang¹, Qing Gao¹, Yuke Ren¹, Jing Guo¹, Lu Zhang¹, Dehua Yang¹, Jingwei Chen¹, Xuan Chang¹, Yanxin Liu^{3,4} , Xingyuan San¹ , Dengyuan Song² & Jianhui Chen^{1,2}

The tunnel oxide passivated contact (TOPCon) solar cell is poised to dominate silicon photovoltaics, yet the atomic-scale nature of pinholes—local disruptions in the SiO_x layer enabling direct conduction—remains unresolved despite its critical importance for device performance. Here, using spherical aberration-corrected transmission electron microscopy, the TOPCon interface is uncovered at the atomic level, revealing two distinct pinhole types: recombinational pinholes with oxygen-depleted Si–Si contacts, and previously unknown passivating pinholes that retain sufficient oxygen to passivate dangling bonds while enabling carrier tunneling. These passivating pinholes exhibit cross-sectional sizes of approximately $1.6 \pm 0.2 \text{ nm} \times 1.4 \pm 0.3 \text{ nm}$ and an area density of $2 \times 10^{12} \text{ cm}^{-2}$. Fischer model analysis demonstrates that pinhole passivation, not geometry, governs device performance. Translating these insights, industrial large-area (333.3 cm^2) TOPCon solar cells achieve certified efficiencies of 25.40% and open-circuit voltages of 738.7 mV. Our findings provide atomic-level insights into the TOPCon interface and offer direct guidance for fabricating high-efficiency solar cells.

Developing a photovoltaic (PV) technology with high-performance, good reliability, low-cost and being environmentally friendly has been an inexorable trend for future energy and carbon neutrality. With the increase of market share (Supplementary Fig. 1)^{1–3}, tunnel oxide passivated contact (TOPCon) solar cells are gradually becoming the mainstream choice of silicon PV technologies because of their high efficiency and being readily into mass production⁴. Recently, the TOPCon cells achieved a rapid progress. In the aspect of power conversion efficiency (PCE), the Fraunhofer Institute for Solar Energy Systems (Fraunhofer-ISE) has achieved a PCE of 26% (4 cm^2) for p-type

TOPCon solar cells, while Jiangsu Runergy New Energy Technology Co., Ltd. (Runergy) has achieved a PCE of 26.55% (335.2 cm^2) for n-type TOPCon solar cells^{5,6}. Recent report shows that JinkoSolar's perovskite stack cells based on n-type TOPCon have a high PCE of 33.24%⁷. In the aspect of the leveled cost of energy (LCOE), a below 0.30 RMB/kWh cost has happened in China² and even 0.07 RMB/kWh in Saudi Arabia^{8,9}. Such alarming numbers make the global PV industry to have truly entered the n-type crystalline Si (c-Si) age, and it is expected that the TOPCon technology will dominate this industry for a 5 years in the future^{1,2,10,11}.

¹Province-Ministry Co-Construction Collaborative Innovation Centre of Hebei Photovoltaic Technology, College of Physics Science and Technology, Hebei University, Baoding, China. ²R&D Department, Das Solar Co., Ltd., Quzhou Green Industry Clustering Zone, Quzhou, China. ³IMD-3 Photovoltaics, Forschungszentrum Jülich GmbH, Jülich, Germany. ⁴Jülich Aachen Research Alliance (JARA-Energy) and Faculty of Electrical Engineering and Information Technology, RWTH Aachen University, Aachen, Germany. ⁵These authors contributed equally: Wenqian Zhang, Kangping Zhang, Yuhua Bai, Yuanyuan Zhang. e-mail: ya.liu@fz-juelich.de; xysan@hbu.edu.cn; d.song@das-solar.com; chenjianhui@hbu.edu.cn

Although the TOPCon cells have such high performance-price ratio and huge industry scale, the understanding of its nature principle is not completely clear. For instance, Peibst et al. have reported arguments that laterally homogenous tunneling might occur in carrier-selective poly-Si/c-Si junctions with an interfacial oxide layer and also in pinhole formation, where it is commonly considered as poor oxygen passivation¹². In particular, the role of the pinholes, where the lattice of the poly-Si is in direct contact with the lattice of c-Si, and carrier transport within pinholes, are still not fully understood. This leads to the PCE of TOPCon solar cells has not yet reached their highest level in technology. The theoretical efficiency limit of single-sided n-type TOPCon solar cells is 27.79%¹³. Especially, open circuit voltage (V_{oc}) and fill factor (FF) to be determined by interface passivation and carrier tunneling, strongly related to the TOPCon interface, including poly-Si, interfacial oxide and pinholes.

The FF of TOPCon cells would depend on two factors: interfacial defect passivation (simultaneously affecting V_{oc}) and carrier tunneling probability. A thicker oxide layer would contribute to better interface passivation but reduce carrier tunneling probability, resulting in decent V_{oc} but low FF¹⁴. Too thin oxide layer would form more pinholes, although they are beneficial to carrier tunneling, but results in poor passivation and eventually both low V_{oc} and FF. The ideal situation is that there is an interfacial oxide layer, being thin enough while possessing sufficient oxygen especially even into pinholes (referred to as “passivating pinholes”). In this case, the passivation effect and carrier tunneling probability will achieve a perfect balance, presenting the high V_{oc} and FF simultaneously in the device. However, in the actual TOPCon production process, after the back alkaline polishing, the surface may appear uneven state of ups and downs, resulting in uneven thicknesses of the oxide layer, and presenting three cases: the oxide layer is thick (>1.7 nm^{12,15}), defect passivation is good but carrier tunneling probability is not the optimal state (*Case 1*); and the oxide layer is thin (<1.3 nm^{16,17}), which brings to two cases: one is the lack of oxygen passivation into the lattice contact between poly-Si and c-Si, forming the recombinational pinholes, detrimental to device performance (*Case 2*); the other is that there are still sufficient oxygen into the lattice contact between poly-Si and c-Si, forming the passivating pinholes, beneficial to device performance (*Case 3*).

Cases 1 and 2 have been extensively studied and demonstrated by high-resolution transmission electron microscopy (HR-TEM)^{12,15–17}. An etching method to determine of pinhole density and electron beam-induced current (EBIC) to visualize current flow through pinholes have also been tried¹⁵. The rupture of the poly-Si/SiO_x/c-Si interface and the oxide layer thicknesses with 1.0–2.2 nm^{15,16,18,19} have been well observed by HR-TEM. Choi et al. observed the nanopite with the cross-sectional size of -0.8 nm \times 11.2 nm and -0.5 nm \times 26.7 nm in the tunnel oxide layer when annealed at a high temperature¹⁹. Liu et al also found that subnanometer pits with the cross-sectional size of -1.5 nm \times 4.6 nm and -1.5 nm \times 7 nm are formed in the oxide layer¹⁶. However, those observations are only nanopites rather than pinholes. Identification of pinholes the poly-Si/SiO_x/c-Si interface is still challenging due to the insufficient resolution of HR-TEM. Therefore, to date, in c-Si PV, *Case 3* has yet to be discovered.

The spherical aberration (C_s)-corrected high-angle annular dark field-scanning transmission electron microscope (HAADF-STEM) is a more advanced technique, from which many atomic-level structure mechanisms, such as the c-Si/a-Si:H interface in silicon heterojunction solar cells, have been uncovered²⁰. In this study, the passivating pinholes, with the cross-sectional size of -1.6 nm \times 1.4 nm, i.e., *Case 3* as state above, are identified at the poly-Si/c-Si interface in large-area, high-PCE and industrial TOPCon solar cells using C_s -corrected HAADF-STEM. The sufficient oxygen is observed into pinholes, corresponding to the high-PCE TOPCon cells. It presents a new understanding that there are actually two types of pinholes, recombinational pinholes and passivating pinholes. The former is as traditionally understood and

reported in the literature, the direct contact of the poly-Si into c-Si leads to large number of dangling bond defects; and the latter is a new discovery that the poly-Si/c-Si interface still has sufficient oxygen passivation on dangling bond defects. This kind of microstructure would not happen in silicon heterojunction (SHJ) solar cells or passivated emitter and rear contact (PERC) solar cells, potentially indicating that the TOPCon cell can possess higher performance, which is consistent with the theoretical result^{13,21}. The guidance for improving PCE of TOPCon industry can be concluded: device optimization should focus on optimizing back polishing surface morphologies, oxide layer processing, and polycrystalline layer processing in order to obtain more passivating holes for trade-off between passivation effects and carrier tunneling probability, simultaneously achieving high V_{oc} and FF. Eventually, the TOPCon solar cell with passivating pinholes present a certified power conversion efficiencies of up to 25.40% and open circuit voltage up to 738.7 mV on industry-grade silicon wafers (total area of 333.3 cm²).

Results

Large-area and high-efficiency tunnel oxide passivated contact solar cells

Figure 1a illustrates the structural diagram of the TOPCon solar cell with passivating pinholes. On the front of the solar cell, a state-of-the-art selective emitter (SE) structure used by industry was implemented. This consisted of a SE by boron diffusion and laser doping, Al₂O₃ passivation and silicon nitride (Si₃N₄) antireflection layer. The SE contributes the suitable junction doping profile with a very low contact resistivity (ρ_c) of -1 m Ω cm² and a low carrier recombination parameter ($J_{0, emitter}$) of <5 fA/cm² simultaneously (Supplementary Fig. 2). On the back of the solar cell, poly-Si junctions are formed by embedding a thin insulating layer of silicon oxide (SiO_x) between the c-Si wafer and a highly doped poly-Si layer. The disruptions in the SiO_x, often referred to as pinholes, with less oxygen and sufficient oxygen, respectively, corresponding to recombinational pinholes and passivating pinholes, are illustrated in Fig. 1a. Using optimized oxidation processes in low-pressure chemical vapor deposition (LPCVD) procedure, (Supplementary Fig. 3) combining with suitable back polishing and poly-Si fabrication, on the quasi-square silicon wafer with the industrial size of 182 mm \times 183.75 mm (Fig. 1b), a high PCE of 25.40% is certified by ISFH with a total area of 333.3 cm² measured under standard test conditions (Fig. 1c). For comparison study, we also fabricated TOPCon cells with a low PCE of 24.07% using the controlled LPCVD oxidation process (Supplementary Fig. 3 and Fig. 1d).

Pinhole microstructures are caused by the thermal oxidation process during LPCVD poly-Si. Thermal oxidation is a critical step to form an ultrathin silicon oxide layer on the wafer surface. The control of the oxygen content of the two different types of pinholes can be achieved by a variety of factors, such as oxidation temperature, time, and gas atmosphere, etc. Here, a two-step oxidation method was used. Firstly, it is oxidized with oxygen at a certain temperature for a period of time to form a thin layer of silicon dioxide. Then, it undergoes a period of oxygen-deficit treatment without the introduction of oxygen. In this case, the formation of passivating pinholes with sufficient oxygen involves a longer oxygen passage time, higher temperature, larger gas flow rate and higher pressure, which is also more conducive to the formation of a uniform and dense oxide layer. During the subsequent diffusion process of POCl₃, a lower deposition temperature and time are conducive to improving the microstructure and crystallinity of the polycrystalline silicon film, thereby reducing the probability of recombinational pinholes occurring at the interface. A detailed description of the fabrication procedure (Supplementary Fig. 3) and systematic variation series of the relevant parameters (Supplementary Table 1) for two kinds of solar cell can be found in the Supporting Information.

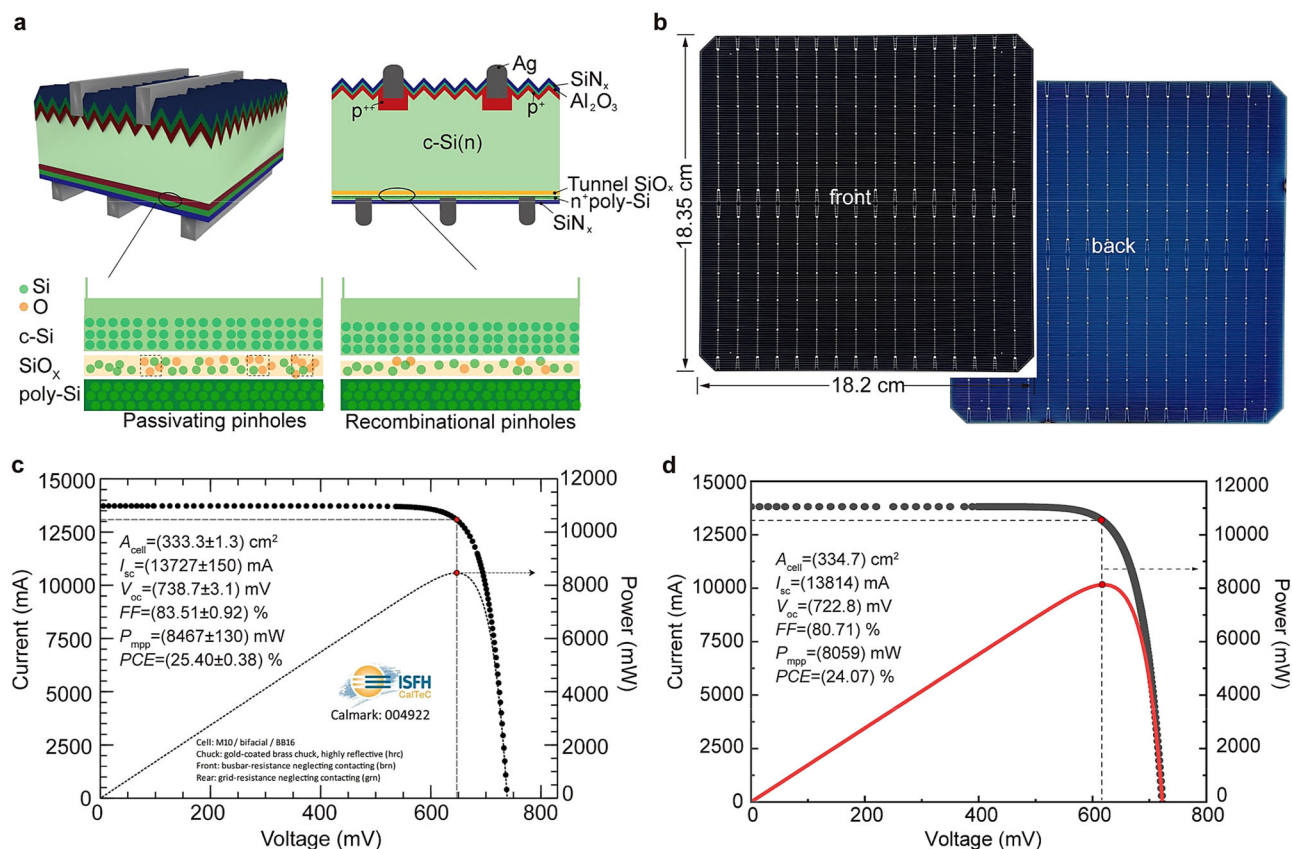


Fig. 1 | Physical structure and electrical properties of TOPCon solar cells.

a Structural diagram of TOPCon solar cell with passivating pinholes. **b** Photograph of TOPCon cell with a size of 183.5 mm x 182 mm. Light I - V curves and PV curves of

(c) champion high-PCE TOPCon solar cell (a PCE of 25.40%) measured by ISFH-CalTeC at an ISO 17025 accredited calibration and test center, and **d** low-PCE cell (a PCE of 24.07%) voltages.

Observation of passivating pinholes and uncovering tunnel oxide passivated contact solar cell interface

Figure 2a, b gives typical cross-sectional HRTEM images of the high-PCE and relatively low-PCE (the controlled one) as stated above, respectively. Only from HRTEM, no obvious difference can be seen between the high-PCE and controlled cell. The poly-Si/ SiO_x /c-Si structure shows uniform interfaces at both sides of the tunnel layer, and an interfacial oxide passivation layer with the thickness of 1.2–1.4 nm is observed. Clearly, this result cannot explain why two devices have obvious performance differences, ΔV_{oc} of -16 mV, ΔFF of -2.8% and ΔPCE of -1.33%.

To further understand the structural characteristics of the TOPCon interface and clarify the difference between the two devices, C_s -corrected HAADF-STEM was performed, as shown in Fig. 2c, d. Through the local contrast variation (Supplementary Fig. 4), we preliminarily determine that the area with brighter contrast corresponds to the location marked with the red box in the C_s -corrected HAADF-STEM diagram, which is the position of the pinhole. Next, we confirmed this phenomenon through STEM-EELS and STEM-EDS. It can be seen that pinholes exist in two TOPCon cell interfaces, and the size of the pinholes can be quantified. C_s -corrected HAADF-STEM imaging reveals two distinct types of nanoscale features: recombinational pinholes, characterized by oxygen-depleted Si-Si direct contact (Fig. 2d, f, h), and passivating pinholes, which retain residual oxygen within the contact region (Fig. 2c, e, g). Pinholes in the high-PCE device have the thickness of 1.55 nm and the size of 1.25 nm, and those in the low-PCE one has the thickness of 1.37 nm and the size of 1.35 nm, respectively. Pinholes were observed in both high-PCE and low-PCE cells (see Supplementary Fig. 5 for more images and Supplementary data 1). Even for the relatively low-PCE TOPCon cell, the pinhole size is

also very small, while high-PCE TOPCon cell has the smaller pinhole, only $\sim 1.55 \text{ nm} \times 1.25 \text{ nm}$ cross-sectional size, which are smaller than the previously reported data^{15,16,19}. More importantly, in the electron energy loss spectroscopy (EELS) distributions, we note that the pinhole in the high-PCE device has still sufficient oxygen into the lattice corresponding to slightly small oxygen-lack valleys (Fig. 2g). This means that defects in the pinhole are passivated by oxygen, leading to a concept being termed the “passivating pinholes”. In contrast, pinhole in the low-PCE device doesn’t have sufficient oxygen (Fig. 2f), with relatively poor passivation effect, which is termed the “recombinational pinholes” as traditionally understood, corresponding to bigger oxygen-lack valleys (Fig. 2h). The similar conclusion can also be proved in the cross-sectional energy-dispersive spectroscopy (EDS) distributions (Supplementary Fig. 6). Clearly, passivating pinholes achieve efficient carrier tunneling while maintaining high-quality interface passivation.

Precise quantification of pinhole size and density remains challenges. The commonly used methods, such as selective etching of the poly-Si layer^{22–25}, conductive atomic force microscopy (c-AFM)²³, and conventional transmission electron microscopy (TEM)^{12,15,23}, suffer from inherent limitations. Selective etching and c-AFM rely on the differential etch rates between Si and SiO_x , but over-etching often leads to coalescence of etch pits, compromising accuracy. More critically, these indirect techniques cannot detect the passivating pinholes identified in this work, as regions with residual oxygen resist etching²⁴. HRTEM is a good choice, but only limited to determine the diameter of $\sim 5 \text{ nm}$ pinholes^{12,22}. Consequently, reported pinhole diameters and densities have historically ranged from ~ 5 to $>200 \text{ nm}$ and pinhole density is 10^6 – $10^8/\text{cm}^2$, respectively (Supplementary Table 2). In this study, we overcome these constraints by employing C_s corrected

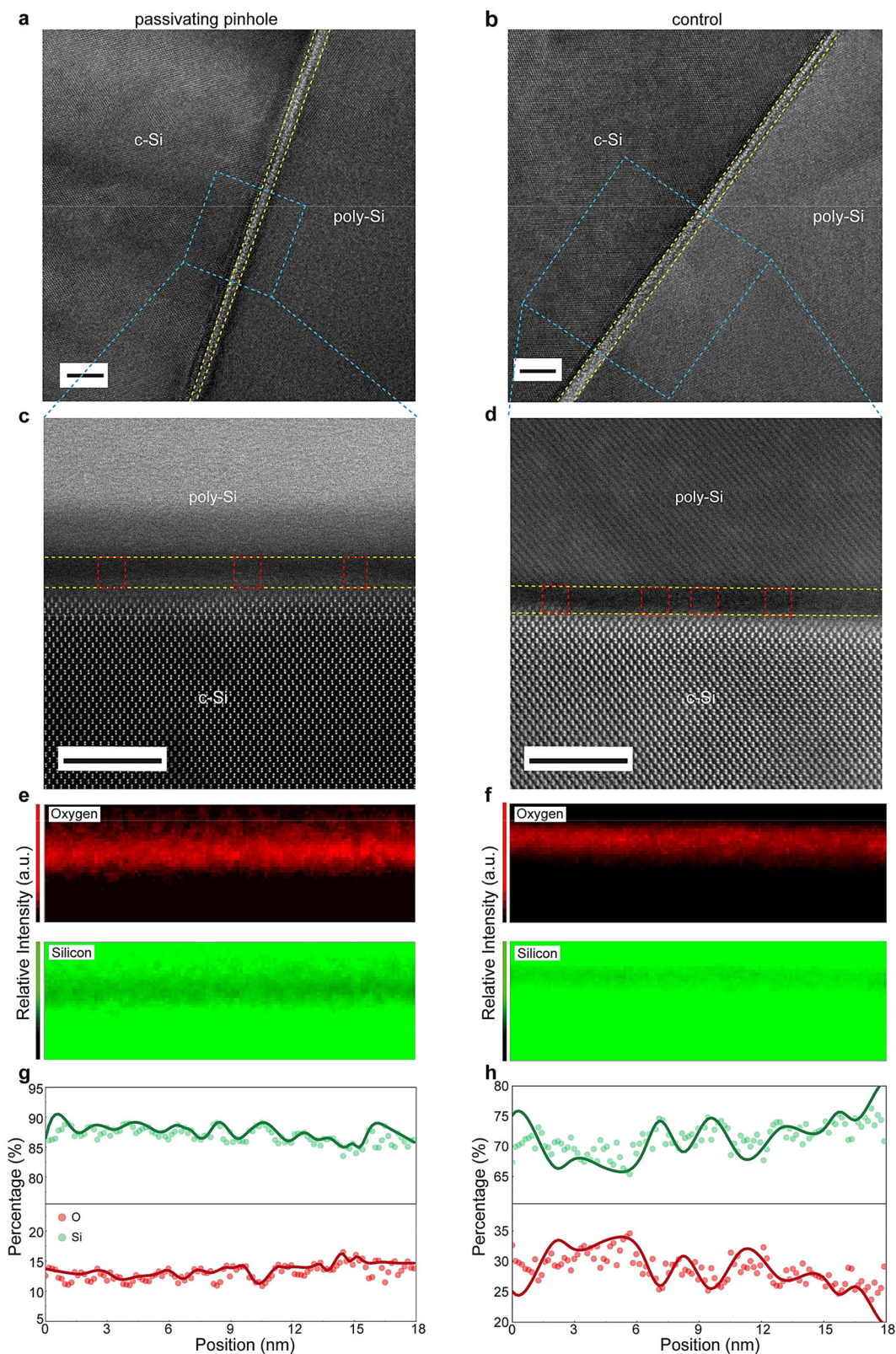


Fig. 2 | Structural characterization of the c-Si/SiO_x/poly-Si interface of TOPCon solar cells. a, b HRTEM images of the c-Si/SiO_x/poly-Si interface of the high-PCE and low-PCE cells, showing local variations in the oxide thickness at the interface. The yellow dashed line indicates the initial oxide interface. **c–h** HAADF-STEM images and EELS measurements of the c-Si/SiO_x/poly-Si interface for high-PCE and low-PCE cells. **c, d** The blue rectangular dashed areas of (a, b), respectively, are shown at higher magnification. The yellow dashed line indicates the magnified

oxide interface, and the red rectangular dashed area indicates the location of the pinhole. **e–h** The O-K side and Si-K side EELS maps of the oxide interface in (c, d), respectively. The elemental content variations are basically corresponding to the pinhole positions in (c, d). The EELS line profiles obtained at similar locations in (g, h) clearly show the presence of oxygen at the passivating pinhole locations. **a–d** Scale bars, 5 nm.

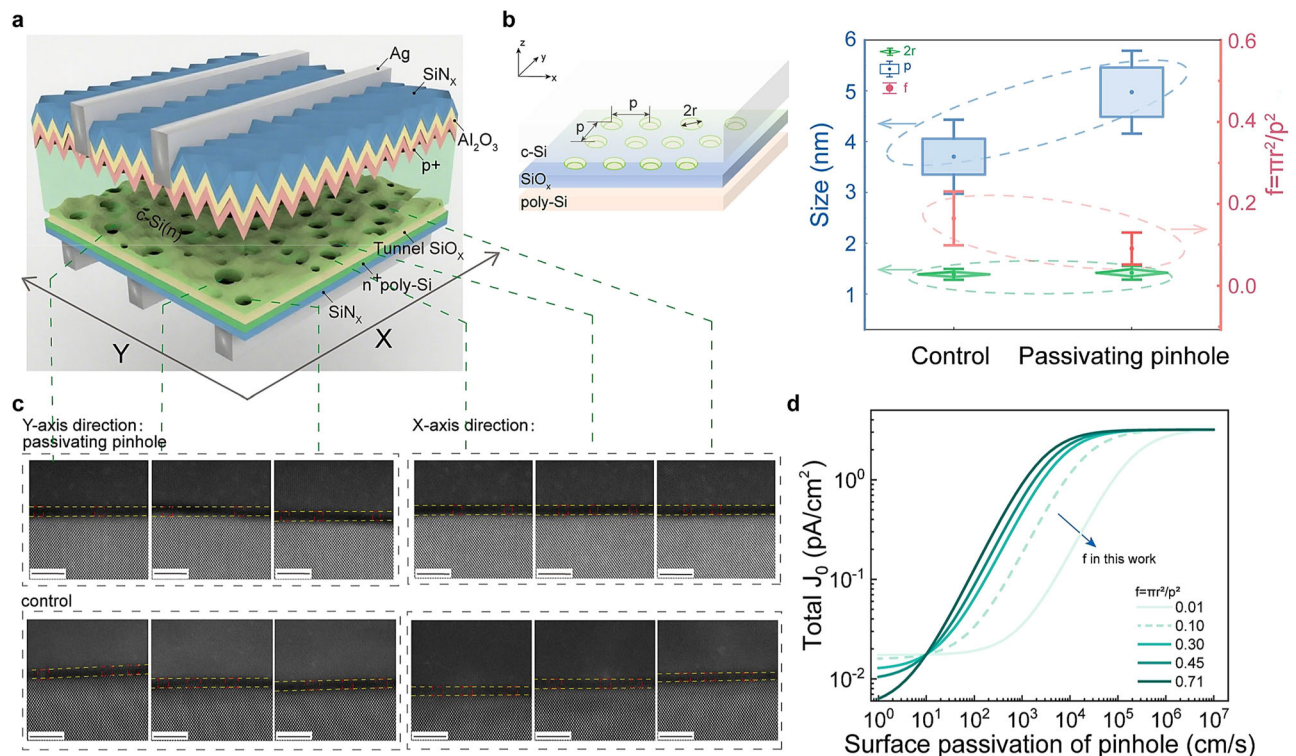


Fig. 3 | Quantification of recombination at the different types of pinholes. **a** X-Y-oriented Cs-corrected HAADF-STEM method and the schematic diagram of pinholes distribution. **b** an approximate Fischer's model geometry and pinhole size statistics. **c** Series of Cs-corrected HAADF-STEM images along the X-axis and Y-axis direction for passivating pinhole cell and recombinational pinhole cell, repetitively. Scale bars, 5 nm. Using this method, pinhole density is generally calculated from

total 40 high-efficiency and low-efficiency solar cells. The calculation is based on assumption that the devices have uniformly distributed pinhole dots with identical surface passivation—it nevertheless provides valuable insight into the underlying trends. **d** The J_0 value under the approximate Fischer geometric model is used as a function of pinhole passivation.

HAADF-STEM, which provides atomic resolution Z contrast imaging. This enables the direct identification of pinholes as small as 1.1–1.8 nm in industrial high-efficiency TOPCon cells. Based on quantified pinholes size, we further proposed an X-Y oriented Cs-corrected HAADF-STEM method, as shown in Fig. 3a. In this approach, we employed X-Y-oriented imaging not as a 3D tomography technique, but as a high-resolution projection method optimized for visualizing and statistically analyzing pinhole features within the SiO_x layer. Since the probability of re-imaging the exact same location along both the X and Y axes on a single specimen is exceedingly low, we sectioned the same solar cell along orthogonal X and Y directions, prepared a statistically significant number of species (Fig. 3c), and derived the pinhole parameters from pooled analysis. Given that the pinholes are sub-2 nm in size—much smaller than the specimen thickness—their projected images in HAADF-STEM remain distinct due to strong Z-contrast, allowing reliable identification and counting. This well-established approach for quantifying nanoscale features in cross-sectional samples is valid provided the features are spatially separated in projection, which is confirmed by our statistical analysis across multiple regions. Using this method, we can statistically sketch pinhole distributions and quantify their areal density. It reveals an unexpectedly high density of 10^{12} cm^{-2} , specifically, $2 \times 10^{12} \text{ cm}^{-2}$ for passivating pinholes and $3 \times 10^{12} \text{ cm}^{-2}$ for recombinational pinholes based on examination of 40 high-efficiency and low-efficiency solar cells (Supplementary Table 3). These values are orders of magnitude greater than those previously reported^{22–25}.

It should be noted, however, that the derived areal density represents a projected estimate. Given the sub-2 nm scale of the pinholes and the typical TEM specimen thickness (~50–150 nm), multiple pinholes may superimpose along the electron-beam direction in

conventional STEM images, potentially influencing quantitative accuracy. To rigorously address this concern, we performed two complementary analyses: (i) 4D-STEM-based ptychographic imaging was performed along the thickness direction, enabling atomic-resolution reconstruction of the c-Si/ SiO_x /poly-Si multilayer structure with atomic resolution (Supplementary Fig. 7 and Fig. 8). While conventional annular dark-field (ADF) imaging enhances Z-contrast and improves pinhole visibility, ptychographic phase reconstruction yields linear contrast, rendering these fine nanoscale features less distinct in the final phase map²⁶; (ii) complementary EELS-mapping was conducted across regions of varying specimen thickness (Supplementary data 2). Quantitative comparison confirmed that pinhole density remains statistically consistent regardless of local thickness, demonstrating that projection-related superposition does not materially distort our spatial distribution analysis, thereby validating the reliability of the quantified ultra-high pinhole densities.

The orders-of-magnitude discrepancy between our measured pinhole density and prior literature values stems not from an artifact, but from a fundamental conceptual shift coupled with advanced methodology. The nanoscale features observed in this study are not the classical “recombinational pinholes”—oxygen-free, direct Si-Si contacts that act as strong recombination centers. Instead, they are predominantly “passivating pinholes”: oxygen-depleted yet oxygen-containing nanodomains (~1.5 nm) that form under optimized, lower-temperature, hydrogen-rich processing conditions. These features act as metastable precursors to classical pinholes, their evolution kinetically arrested to preserve passivation, as supported by recent molecular dynamics simulations²⁷. Therefore, the several orders of magnitude difference in density can be attributed to three synergistic factors: (i) conceptual distinction: a previously inaccessible population

of passivating nano defects is detected, being distinct from terminal recombinational pinholes. (ii) sample state: prior studies often examined test structures or moderate-efficiency precursors, whereas our analysis probes fully optimized, industry-leading devices (>25% efficiency). (iii) detection method: atomic-resolution HAADF-STEM directly images and counts these sub-2 nm, partially oxygenated regions, which are invisible to indirect, diffraction-limited, or etching-based techniques.

This revised understanding resolves an apparent contradiction with prior simulations, such as those by Peibst et al.¹², which suggested that high pinhole densities would be detrimental to performance. That conclusion logically applies to recombinational pinholes. Our findings reveal that in high-performance TOPCon cells, the interfacial landscape is dominated by an ultra-dense array of passivating pinholes. Their exceptional passivation quality (due to residual oxygen) and minimal size together enable efficient carrier tunneling without triggering significant recombination. Thus, the key to high performance is not the absence of pinholes, but the passivation of pinholes—a paradigm shift that aligns our experimental findings with superior device metrics.

The pinholes observed in this work act as localized dot contacts between the crystalline Si wafer and the poly-Si layer. To assess their impact, we quantified the contribution of surface recombination and pinhole area fraction to the saturation current density J_0 using Fischer's analytical model. Based on our quantification of recombination at the size and density of pinholes, an approximate Fischer's model geometry is established^{12,28}, as shown in Fig. 3b, the pinhole fraction is defined, $f = \pi r^2 / P^2$, with r being the point radius and P being the period length of the pinhole distribution, which is actually related to the pinholes' geometry distribution. While the direct application of this model to TOPCon structures has certain limitations—Fischer assumes uniformly distributed dots with identical surface passivation, whereas in real TOPCon cells, pinholes are irregular and heterogeneous contacting, with poly-Si—it nevertheless provides valuable insight into the underlying trends.

The modeling reveals that for a given pinhole geometry, the total J_0 is predominantly controlled by the surface recombination velocity (S) at the pinholes, rather than by their areal fraction alone. This underscores that passivation quality, not pinhole geometry, is the critical factor governing device performance (Fig. 3b, d). Specifically, higher pinhole fractions shift this transition toward lower S -values, rendering J_0 more sensitive to the pinhole surface properties. For the experimentally observed case with $f \approx 0.1$, J_0 increases sharply once $S \geq 10^3$ cm/s, and then saturates at a high level above $S \approx 10^5$ cm/s. When the pinhole fraction is reduced by an order of magnitude (from $f = 0.1$ to $f = 0.01$), the onset of this rapid increase shifts to higher recombination velocities ($S \sim 10^4$ cm/s), indicating a reduced sensitivity of J_0 to the pinhole recombination (Fig. 3d). It can be summarized: (i) the geometry of pinholes (J_0 vs. f) is not the key of high performance of the TOPCon cells, but the passivation of pinholes is a truly key technology; (ii) larger or more pinholes require higher passivation level; (iii) for the passivating pinhole cells, higher pinhole density would lead to lower contact resistance. Thus, passivating pinholes are very necessary and meaningful for the next breakthrough in the TOPCon solar cell community.

The excellent passivation properties and large-area uniformity

Using the technique of the transient photoconductance decay (PCD), the minority carrier lifetime for silicon wafers coated symmetrically with poly-Si/SiO_x layer using corresponding the high-PCE and controlled process was measured and shown in Fig. 4a. Clearly, the sample using the high-PCE process has high effective carrier lifetime (τ_{eff}) of 8.9 ms and that using the low-PCE has relatively low τ_{eff} of 2.96 ms. Saturation current densities, J_0 , were also deduced from PCD measurements according the following Eq. 1, and these were 2.6 and

10.6 fA/cm² for the high-PCE and controlled one, respectively (Fig. 4b).

$$1/\tau_{\text{eff}} = 1/\tau_{\text{bulk}} + 2J_{0,\text{back}}(\Delta n + N_D)/qn_i^2 W \quad (1)$$

Where the effective minority carrier lifetime of the silicon wafer is denoted by τ_{eff} , the bulk lifetime of the silicon material is denoted by τ_{bulk} , the backfield saturation current density is denoted by $J_{0,\text{back}}$, the carrier concentration change is denoted by Δn , the bulk doping concentration is denoted by N_D , the charge amount is denoted by q , the intrinsic carrier concentration is denoted by n_i , and the silicon wafer thickness is denoted by W .

The excellent passivation quality directly explains the higher V_{oc} achieved in cells with passivating pinholes (Fig. 1). Note that the measured difference in V_{oc} between high- and low-PCE cells is 15.9 mV. Based solely on the difference in their recombination current densities ($J_0 = 2.60$ vs. 10.64 fA cm⁻²), the expected ΔV_{oc} is only -11 mV, leaving a residual of -5 mV unaccounted for. We attribute this additional voltage gain to an improvement in the bulk Shockley–Read–Hall (SRH) lifetime induced by the optimized junction-formation process. As highlighted by Krügener et al.²⁹, the formation of n-type poly-Si on oxide junctions under optimal conditions not only minimizes interface recombination (J_0) but also promotes effective gettering of metal impurities, thereby enhancing the bulk SRH lifetime. In our high-PCE cells, the same optimized annealing that fosters passivating pinholes also facilitates this beneficial gettering. Thus, the total V_{oc} advantage stems from the synergistic improvement of both interface and bulk properties—a hallmark of advanced TOPCon processing that is critical for surpassing 25% efficiency.

A highly spatial resolution of photoluminescence (PL) mapping was performed on the 333.3 cm² industrial size solar cell, as shown in Fig. 4c, d, a homogenous contrast throughout all measurements in both two cells, but higher PL intensity on the passivating pinhole cell are observed, indicating that a lower number of interfacial defects exist in the passivating pinhole cell. Furthermore, a Corescan tool was employed to scan the V_{oc} spatial distribution of two cells (Fig. 4e, f). Corescan is an instrument to diagnose the problems of the devices through different measurement modes^{30,31}. The similar large-area uniformity and an obvious promotion of the V_{oc} on the passivating pinhole cell are proved.

The difference in FF is still associated with series resistance and, furthermore, contact resistance. Suns- V_{oc} measurement of the solar cell is performed to obtain the pseudo fill factor ($p\text{FF}$) and series resistance (R_s), as shown in Fig. 4g. It can be seen that the difference of $p\text{FF}$ between high-PCE and low-PCE cell is 0.61%, lower than the difference of FF between high-PCE and low-PCE cell (2.8%). Such big difference is related to the difference of series resistance (R_s) between the two samples (357 and 619 mΩ cm² for the high-PCE and low-PCE solar cells, respectively, measured by a series-resistance-free method³², see the supplementary Fig. 9), which is mainly determined by the charge carrier transport across the SiO_x/poly-Si junction on the rear. We employed a TLM method to evaluate the contact resistivity (ρ_c), as shown in Fig. 4h, the high-PCE cell has a ρ_c of 4.6 mΩ cm² and the low-PCE cell has a ρ_c of 5.4 mΩ cm², respectively. Only according to pinhole density affecting ρ_c , this is inconsistency (Fig. 3). In order to clarify this point, we have studied the diffusion behavior difference of phosphorus dopants from the poly-Si into the wafer near the pinholes (Supplementary Fig. 10a, b). It can be seen that phosphorus diffusion happens across the recombinational pinholes, but is effectively barred near the passivating pinholes. The phosphorus diffusion behavior difference leads to different doping profile (see supplementary Fig. 10c) and then affects contact resistance.

Discussion

In summary, this work successfully unveils the TOPCon cell interface at the atomic level, revealing two distinct types of pinholes:

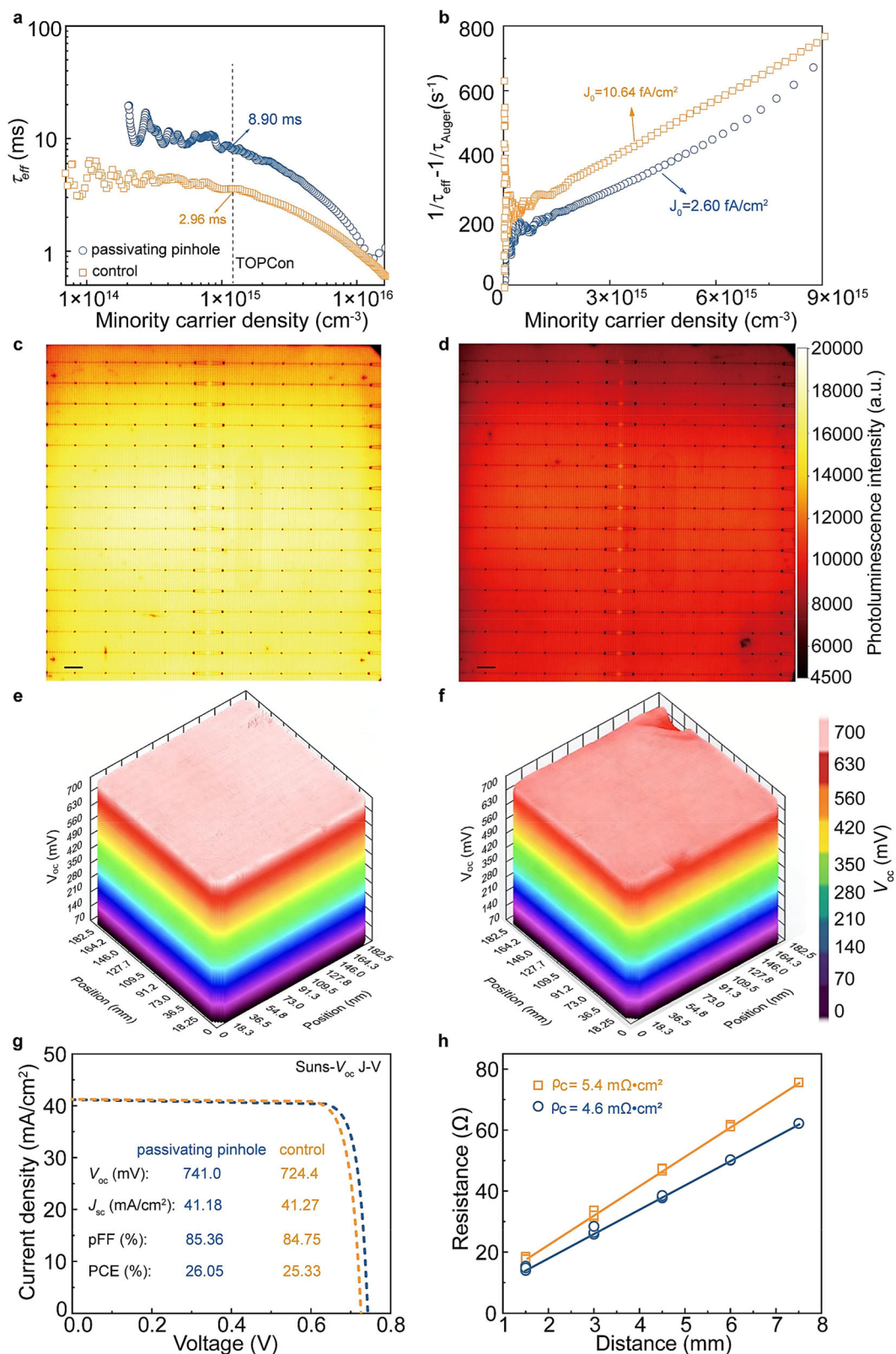


Fig. 4 | Passivation performance and large area uniformity of TOPCon solar cells. **a** τ_{eff} of high-PCE and low-PCE cells corresponding to the preparation of two-sided $\text{SiO}_x/\text{poly-Si}(\text{n}^+)$ symmetric samples on n-Si 1–3 Ωcm two-sided polished substrates. τ_{eff} is 8.90 ms for high-PCE cell samples and 2.96 ms for low-PCE cell samples for a carrier injection level of $5 \times 10^{15} \text{ cm}^{-3}$. **b** J_0 of high-PCE and low-PCE cells calculated from the relationship of the injected concentration and the J_0

calculated from the relationship between τ_{eff} . **c, d** PL of the high-PCE and low-PCE cells, the PL of the high-PCE cell is stronger and has fewer surface defects. Scale bars, 10 mm. **e, f** V_{oc} scans of the high-PCE and low-PCE cells, the high-PCE cell has higher V_{oc} homogeneity. **g** I - V curves measured by a Suns- V_{oc} method and **h** contact resistivity of two types of solar cells measured by TLM.

recombinational pinholes, which lack oxygen passivation and lead to direct Si–Si contact with high defect density, and passivating pinholes, which retain sufficient oxygen to passivate dangling bonds while enabling efficient carrier tunneling. The identification of passivating pinholes represents a paradigm shift in understanding TOPCon interface physics, highlighting that high device performance stems not from the absence of pinholes but from their effective passivation. The atomic-scale insights, coupled with the development of a robust quantification methodology using Cs-corrected HAADF-STEM, provide direct guidance for industrial fabrication of high-efficiency, large-area TOPCon solar cells. Future work may focus on the controlled formation of passivating pinholes through optimized oxidation and annealing processes, as well as extending this understanding to TOPCon-based tandem architectures (such as TOPCon-BC and perovskite/TOPCon tandem solar cells).

Methods

Tunnel oxide passivated contact solar cell fabrication

In this study, we first immersed c-Si wafers in a KOH solution to remove the damage produced during sawing and to form surfaces with random pyramidal structures. Subsequently, the wafers were immersed in hydrochloric acid (HCl) and hydrogen peroxide (H_2O_2) solutions to remove metal ions and hydrofluoric acid (HF) to remove the oxide layer. Uniform p⁺ emitters were formed by successive high-temperature injection and oxidation processes in a gaseous B diffusion tube. In order to form locally redoped selective emitters (SE), a laser was utilized to scan the localized area covered by the metal grid lines, and then the borosilicate glass (BSG) layer was removed, thus avoiding the complicated process of using selective masks. A high-temperature annealing method was used to repair the damage produced during the laser treatment. The backside BSG layer was removed by floating the c-Si wafer on the surface of HF solution, and then the c-Si wafer was immersed in KOH solution for backside polishing. Ultrathin tunneling SiO_x layers were prepared by plasma thermal oxidation. Intrinsic polysilicon was deposited using LPCVD and later diffused in a tube furnace to form doped polysilicon. Afterwards, front and side phosphor-silicon glass (PSG) was removed by a chain cleaning process. The front and side polysilicon layers are removed by polishing with KOH solution. The front-side BSG and back-side PSG were removed by wet over HF. Al_2O_3 and $\text{SiN}_x\text{:H}$ stacked coatings were deposited on both sides of the wafers using atomic layer deposition (ALD) and plasma-enhanced chemical vapor deposition (PECVD) techniques, respectively. In the metallization stage, silver/aluminum electrodes were screen-printed on the front side, and silver electrodes were screen-printed on the back side. Finally, the entire structure is sintered in a belt furnace at 830 °C to complete the solar cell fabrication process.

Electrical characterization of the solar cells

Internal 1-sun current–voltage (I – V) solar cell parameters were measured under standard test conditions (AM 1.5 G, 100 mW cm^{-2} , 25 °C) using a sun simulator. Based on certified I – V current calibration measurements (ISFH test) and verified light J – V curves of the solar cells, gold-coated brass chuck was used to mount the solar cells, and the resistance of the back-side grid and the front-side busbar were neglected. The contact resistivity of different samples was determined by the transfer length method (TLM). According to the theory of TLM, the contact resistivity can be extracted from the intercept of a linear fit, whereas the sheet resistance of the substrate can be extracted from the slope.

Microstructural analysis of the solar cells by aberration-corrected transmission electron microscopy

Several long rectangular specimens of 2.3–2.7 mm in length and 0.8–1.2 mm in width were cut by a diamond wire cutter and counter-

bonded with 4–6 pieces. Silicon carbide (SiC) paper was used to grind the cross sections of the counterbonded samples to ~30 μm , and the cross sections were pasted onto a 3 mm diameter molybdenum mesh. We prepared a large number of TEM samples from different directions along the orthogonal X and Y axes of the same cell and analyzed them en masse to yield statistically robust metrics. The TEM samples for the experiments were obtained by argon ion thinning in a Gatan Precision Ion Polishing System (PIPS) using a single gun.

High-angle annular dark-field scanning transmission electron microscope (HAADF-STEM) images were recorded using aberration-corrected transmission electron microscopes (JEM ARM200F), a microscope operating at 200 kV with a cold-field emission gun, a probe corrector, and a dual-silicon drift detector; and the Spectra 300 (Thermo Fisher Scientific), a 300 kV monochromator configured with a high-speed (Super-X EDS detector). Electron energy loss spectroscopy (EELS, Gatan continuum 1069) measurements were performed in STEM mode. The HAADF-STEM data and EELS data were analyzed using GMS software. For each case, a large number of observations and corresponding EDS as well as EELS analyses were carried out for individual specimens and for different locations of various specimens to show the reproducibility of the results. Absolute thickness of EELS specimen is calculated through the Log-ratio (absolute) method and the inelastic mean free path³³, the parameters are as follows, convergence semi-angle (mrad) is 69.22, collection semi-angle (mrad) is 207.66.

We quantified the linear pinhole density along the X and Y directions in single HAADF-STEM image. We then conducted statistical analysis on a certain amount of measurement results and multiplied the linear densities in these two directions to obtain the projected density within the entire cell region.

Details of 4D data acquisition and ptychographic reconstruction

The 4D data was collected using an operating voltage of 200 kV, a convergence semi-angle of 25.3 mrad and an underfocus of 20 nm. The 4D data had a scanning step size of 0.4 Å, and each scanning point's CBED pattern consisted of 104×104 pixels, with a pixel size of 0.04181/Å. To achieve a pixel size of 0.133 Å in the real space of reconstructed phases, each CBED was expanded to 180×180 pixels during the reconstruction process. Six probe states and 16 object slices were used in the reconstruction process, with each slice of the object having a thickness of 0.9 nm. The ptychographic reconstruction was performed based on the APP algorithm.

Characterization of passivation quality

Photoluminescence (PL) measurements using a PL tester (LIS-R, BT Imaging Pty Ltd.) to extract carrier recombination and passivation properties. A Vovscan test system (SunLab SCRA1-9001, the Netherlands) was used to scan the cell frontal V_{oc} and obtain the cell V_{oc} distribution map to detect whether the cell achieves large area uniformity preparation. A Sinton WCT-120 lifetime tester was utilized to measure double-sided SiO_2 /poly-Si(n^+) symmetric samples prepared on double-sided polished n-Si substrates with conductivity 1–3 Ω cm. From these measurements, we obtained the implied open-circuit voltage (iV_{oc}) at one sun, the saturation current density (j_0) at an excess carrier density of $5 \times 10^{15} \text{cm}^{-3}$ and the effective minority carrier lifetime (τ_{eff}) at a carrier density of $1 \times 10^{15} \text{cm}^{-3}$.

Reporting summary

Further information on research design is available in the Nature Portfolio Reporting Summary linked to this article.

Data availability

All relevant data that support the findings of this study are presented in the manuscript and Supplementary Information file. Source data are provided with this paper.

References

- Markus, F. et al. 2023 Results Including Maturity Report. *International Technology Roadmap for Photovoltaics (ITRPV)*, <https://www.qualenergia.it/wp-content/uploads/2024/06/ITRPV-15th-Edition-2024-2.pdf> (2024).
- S. W. et al. China PV industry development roadmap(2023-2024), *China Photovoltaic Industry Association(CPIA)*, https://www.chinapv.org.cn/Industry/resource_1380.html (2024).
- Vicari Stefani, B. et al. Historical market projections and the future of silicon solar cells. *Joule* **7**, 2684–2699 (2023).
- Zhou, J. K. et al. Data-driven tunnel oxide passivated contact solar cell performance analysis using machine learning. *Adv. Mater.* **36**, <https://doi.org/10.1002/adma.202309351> (2024).
- Richter, A. et al. Design rules for high-efficiency both-sides-contacted silicon solar cells with balanced charge carrier transport and recombination losses. *Nat. Energy* **6**, 429–438 (2021).
- Runergy Research Institute, ISFH Germany, “Runergy Achieves 26.55% Full-Area N-Type Cell Efficiency, Setting A New World Record” *Runergy*, <https://www.runergy.com/runergy-achieves-26-55-full-area-n-type-cell-efficiency-setting-a-new-world-record/> (2025).
- JinkoSolar Holding Co., Ltd, “JinkoSolar’s Perovskite Tandem Solar Cell Based on N-type TOPCon Sets New Record with Conversion Efficiency of 33.24%” *PR Newswire*, <https://www.prnewswire.com/news-releases/jinkosolars-perovskite-tandem-solar-cell-based-on-n-type-topcon-sets-new-record-with-conversion-efficiency-of-33-24-302160546.html> (2024).
- King Abdullah Petroleum Studies and Research Center (KAPSARC), “Future Trends in Electricity Demand in Saudi Arabia and the Gulf Region” *KAPSARC*, <https://www.kapsarc.org/>, <https://doi.org/10.30573/ks-2021-wb05> (2021).
- Asia Photovoltaic Exhibition, “1.04 cents/KWH, a new low in the world electricity price, Saudi Arabia signed seven new photovoltaic power plant purchase agreement” *International Energy Network*, <https://www.in-en.com/article/html/energy-2303223.shtml> (2021).
- Y.T., “Consensus of many global authorities: TOPCon technology dominates the market, and LCOE leads the industry to return to core values” *China Energy Network*, https://www.cnenergynews.cn/guangfu/2024/09/30/detail_20240930178163.html (2024).
- JA Solar Technology Co., Ltd, “JA Technology CTO comprehensive interpretation: the underlying advantages and future form of TOPCon technology” *Solarbe*, <https://news.solarbe.com/202408/19/381383.html> (2024).
- Peibst, R. et al. Working principle of carrier selective poly-Si/c-Si junctions: Is tunnelling the whole story? *Sol. Energy Mater. Sol. Cells* **158**, 60–67 (2016).
- Su, Q. et al. Theoretical limiting-efficiency assessment on advanced crystalline silicon solar cells with Auger ideality factor and wafer thickness modifications. *Prog. Photovolt. Res. Appl.* **32**, 587–598 (2024).
- Razaq, A., Allen, T. G. & De Wolf, S. Design criteria for silicon solar cells with fill factors approaching the Auger limit. *ACS Energy Lett.* **8**, 4438–4440 (2023).
- Guthrey, H. et al. Effect of surface texture on pinhole formation in SiO_x-based passivated contacts for high-performance silicon solar cells. *ACS Appl. Mater. Interfaces* **12**, 55737–55745 (2020).
- Liu, W. et al. Polysilicon passivating contacts for silicon solar cells: interface passivation and carrier transport mechanism. *ACS Appl. Energy Mater.* **2**, 4609–4617 (2019).
- Glunz, S. W. et al. Silicon-based passivating contacts: the TOPCon route. *Prog. Photovolt. Res. Appl.* **31**, 341–359 (2021).
- Köhler, M. et al. A silicon carbide-based highly transparent passivating contact for crystalline silicon solar cells approaching efficiencies of 24%. *Nat. Energy* **6**, 529–537 (2021).
- Choi, S. et al. Structural evolution of tunneling oxide passivating contact upon thermal annealing. *Sci. Rep.* **7**, 12853 (2017).
- Qu, X. et al. Identification of embedded nanotwins at c-Si/a-Si:H interface limiting the performance of high-efficiency silicon heterojunction solar cells. *Nat. Energy* **6**, 194–202 (2021).
- Schmidt, J., Peibst, R. & Brendel, R. Surface passivation of crystalline silicon solar cells: present and future. *Sol. Energy Mater. Sol. Cells* **187**, 39–54 (2018).
- Tetzlaff, D. et al. A simple method for pinhole detection in carrier selective POLO-junctions for high efficiency silicon solar cells. *Sol. Energy Mater. Sol. Cells* **173**, 106–110 (2017).
- Lancaster, K., Groß, S., Feldmann, F., Naumann, V. & Hagendorf, C. Study of pinhole conductivity at passivated carrier-selected contacts of silicon solar cells. *Energy Procedia* **92**, 116–121 (2016).
- Feldmann, F. et al. A study on the charge carrier transport of passivating contacts. *IEEE J. Photovolt.* **8**, 1503–1509 (2018).
- Wietler, T. F. et al. Pinhole density and contact resistivity of carrier selective junctions with polycrystalline silicon on oxide. *Appl. Phys. Lett.* **110**, 253902 (2017).
- Sha, H., Cui, J. & Yu, R. Deep sub-angstrom resolution imaging by electron ptychography with misorientation correction. *Sci. Adv.* **8**, eabn2275 (2022).
- Diggs, A. et al. Pinhole formation by nucleation-driven phase separation in TOPCon and POLO solar cells: structural dynamics and optimization. *ACS Appl. Energy Mater.* **7**, 3414–3423 (2024).
- Plagwitz, H. & Brendel, R. Analytical model for the diode saturation current of point-contacted solar cells. *Prog. Photovolt. Res. Appl.* **14**, 1–12 (2006).
- Krügener, J. et al. Improvement of the SRH bulk lifetime upon formation of n-type POLO junctions for 25% efficient Si solar cells. *Sol. Energy Mater. Sol. Cells* **173**, 85–91 (2017).
- van der Heide, A. S. H., Schönecker, A., Bultman, J. H. & Sinke, W. C. Explanation of high solar cell diode factors by nonuniform contact resistance. *Prog. Photovolt. Res. Appl.* **13**, 3–16 (2005).
- van der Heide, A. S. H., Bultman, J. H., Hoornstra, J. & Schönecker, A. Error diagnosis and optimisation of c-Si solar cell processing using contact resistances determined with the corescanner. *Sol. Energy Mater. Sol. Cells* **74**, 43–50 (2002).
- Wolf, M. & Rauschenbach, H. Series resistance effects on solar cell measurements. *Adv. Energy Convers.* **3**, 455–479 (1963).
- Malis, T., Cheng, S. C. & Egerton, R. F. EELS log-ratio technique for specimen-thickness measurement in the TEM. *J. Electron Microsc. Tech.* **8**, 193–200, (1988).

Acknowledgements

This work was financially supported by the National Natural Science Foundation of China (52402048, 62274054), Hebei Provincial Innovation Capability Enhancement Program Project (24464302D), Natural Science Foundation of Hebei Province (F2023201001; F2023201005), Hebei Province Department of Education Youth Fund Project (No. QN2025349), Interdisciplinary research project of Hebei University (DXK202303), the Central Guidance on Local Science and Technology Development Fund Project of Hebei Province (No. 236Z4307G), Hebei province Science Foundation for Distinguished Young Scholars (F2021201035). The “Pioneer” and “Leading Goose” Research & Development Program of Zhejiang Province (Grant No. 2024C01054). The Natural Science Interdisciplinary Research Program of Hebei University (Grant No. DXK202305).

Author contributions

J.C. conceived and supervised this study. D.S., K. Z. conducted device fabrication and photovoltaic measurements. X.S. conducted aberration-corrected HRTEM and 4D-STEM. Y.L. carried out the simulation. Y.Z., K.Y., characterized aberration-corrected HRTEM images of devices. W.Z., Y.B. characterized and analyzed all data. L. Li, J. Li, Y. Sun, and Y.

Wu conducted in solar cell measurements. Q. Gao and Y. Ren conducted the contact resistance measurements. B.C., X.Y., X.Z., J.G., L.Z., D.Y., J.C., and X.C. participated in the important discussion. J.C., W.Z., and Y.B. wrote the first draft of the manuscript. D.S., Y.L., and X.S. help to improve the manuscript writing and contribute to the important discussions. All authors contributed to discussions and commented on the manuscript. J.C., D.S. directed the project. The manuscript was prepared, revised, and finalized by J.C., W.Z., X.S., Y.L., and D.S.

Competing interests

The authors declare no competing interests.

Additional information

Supplementary information The online version contains Supplementary material available at <https://doi.org/10.1038/s41467-026-70511-2>.

Correspondence and requests for materials should be addressed to Yanxin Liu, Xingyuan San, Dengyuan Song or Jianhui Chen.

Peer review information *Nature Communications* thanks Robby Peibst and the other anonymous reviewer(s) for their contribution to the peer review of this work. A peer review file is available.

Reprints and permissions information is available at <http://www.nature.com/reprints>

Publisher's note Springer Nature remains neutral with regard to jurisdictional claims in published maps and institutional affiliations.

Open Access This article is licensed under a Creative Commons Attribution-NonCommercial-NoDerivatives 4.0 International License, which permits any non-commercial use, sharing, distribution and reproduction in any medium or format, as long as you give appropriate credit to the original author(s) and the source, provide a link to the Creative Commons licence, and indicate if you modified the licensed material. You do not have permission under this licence to share adapted material derived from this article or parts of it. The images or other third party material in this article are included in the article's Creative Commons licence, unless indicated otherwise in a credit line to the material. If material is not included in the article's Creative Commons licence and your intended use is not permitted by statutory regulation or exceeds the permitted use, you will need to obtain permission directly from the copyright holder. To view a copy of this licence, visit <http://creativecommons.org/licenses/by-nc-nd/4.0/>.

© The Author(s) 2026